



Photoredox coupling of benzyl alcohol oxidation with CO₂ reduction over CdS/TiO₂ heterostructure under visible light irradiation

Ming-Yu Qi¹, Qiong Lin¹, Zi-Rong Tang^{*}, Yi-Jun Xu^{2,*}

College of Chemistry, State Key Laboratory of Photocatalysis on Energy and Environment, Fuzhou University, Fuzhou 350116, PR China



ARTICLE INFO

Keywords:
CO₂ reduction
C–C coupling
Heterostructure
Visible light
Anti-photocorrosion

ABSTRACT

Coupling CO₂ photoreduction with selective organic synthesis offers a promising modus operandi to enable simultaneous utilization of photogenerated electrons and holes to realize solar fuels production and chemicals synthesis. Herein, we report a bifunctional zero-dimensional cadmium sulfide quantum dots-two-dimensional titanium dioxide nanosheets (CdS/TNS) heterostructure for photoredox-catalyzed coupling of C–C bond synthesis via selective oxidation of benzyl alcohol with CO₂ photoreduction to CO under visible light. The compositing heterointerface is beneficial for the adsorption and activation of CO₂, thereby promoting the photoreduction of CO₂. Remarkably, the synergistic interaction between CdS and TNS tunes the selectivity of benzyl alcohol oxidation from carbonyl compound to the C–C coupled products. Mechanistic studies unveil that the generation of C–C coupled products processes via key radical •CH(OH)Ph intermediates. Theoretical simulations reveal that the weaker adsorption of •CH(OH)Ph radical over CdS/TNS than bare CdS contributes to the formation of highly selective C–C coupled products. The findings are expected to offer instructive guidance on rationally designing the dual-functional catalysts with efficient photoredox-catalyzed coupling reaction systems for integrating CO₂ reduction with selective organic transformations.

1. Introduction

Catalytic reduction of carbon dioxide (CO₂) into usable fuels by solar energy has been regarded as an appealing approach to mitigate the greenhouse effect and energy crisis [1–6]. Most CO₂ photoreduction studies focus on the reductive half-reaction, but pay less attention to the oxidative half-reaction [7–11]. Merging oxygen (O₂) production via oxidation from pure water with the CO₂ reduction is an ideal reaction [1, 12]; nevertheless, the release of O₂ is difficult and rarely reported because of sluggish reaction kinetics involving the cleavage of four O–H bonds and its difficult desorption [7]. Furthermore, such catalytic systems for CO₂ photoreduction with pure water often suffers from low activity/selectivity and poor stability. To balance these issues, sacrificial reagents (triethanolamine (TEOA), isopropyl alcohol, sodium sulfite and ascorbic acid, etc.) are usually used to capture holes to accelerate the catalytic rate, which inevitably wastes the oxidative capacity of holes, and produces the unwanted oxidation products [4,13]. On the contrary, replacing holes scavengers with biomass-derived alcohols and other platform molecules could not only produce high value-added chemicals,

but also efficiently cut the cost of CO₂ reduction, thereby realizing the concurrent CO₂ photoreduction and selective organic oxidation [13–17].

Selective conversion of benzyl alcohol (BA) to corresponding carbonyl compounds or C–C coupled products via photocatalysis provides a sustainable appealing pathway to obtain high-value chemicals [18]. Thus far, in most instances of photocatalytic BA transformation, benzaldehyde (BAD) is formed as a major product with semiconductor-based photocatalysts [19–22], while few reports are accomplished on the selective C–C coupling synthesis from BA oxidation. For instance, Weiss's group has reported the oxidation of BA to C–C coupled products over CdS quantum dots (QDs) [23], featuring a low selectivity with multiple products of deoxybenzoin, benzil, and hydrobenzoin. The coproduction of C–C coupled products and hydrogen (H₂) has also been realized on Zn_xIn₂S_{3+x} [24], but suffering from the poor selectivity for each C–C coupled product. The photoredox-catalyzed dehydrocoupling of BA into hydrobenzoin and H₂ over the SiO₂-supported CdS QDs has also been reported by our group [25], but the underlying reason for the high selectivity of C–C coupled

* Corresponding authors.

E-mail addresses: zrtang@fzu.edu.cn (Z.-R. Tang), yjxu@fzu.edu.cn (Y.-J. Xu).

¹ These two authors contribute equally to this work.

² Webpage: <http://xugroup.fzu.edu.cn>

product remains elusive.

Recent surge of integrating CO_2 photoreduction with oxidative organic transformations in a photoredox-catalyzed reaction system demonstrates a fascinating modus operandi that enables full and simultaneous utilization of photoexcited electrons and holes to achieve the economical and environmentally benign goal [4,13,26]. In this regard, it is crucial to rationally design composite photocatalysts with the suitable band structure and heterointerface for redox half-reaction, efficient charge carrier separation and reactive sites for such cooperative coupling of CO_2 photoreduction and selective organic transformations in one redox cycle.

Herein, we report CdS QDs- TiO_2 nanosheets (CdS/TNS)-based bifunctional catalytic system toward visible light-driven CO_2 reduction to carbon monoxide (CO) and simultaneous dehydrocoupling of BA to hydrobenzoin and benzoin that are the versatile building blocks in pharmaceutical intermediates [25,27] in one photoredox cycle. It is worth mentioning that anchoring CdS QDs onto TNS not only effectively inhibits the recombination of photogenerated carriers, but also greatly increases the anti-photocorrosion capability of CdS , thereby boosting the visible-light photoredox-catalyzed activity and the durability of CdS/TNS composite. The synergy between CdS and TNS significantly favors the adsorption and activation of CO_2 , and simultaneously tunes the product selectivity from BAD to hydrobenzoin and benzoin. Mechanistic studies suggest that the C-C coupling synthesis occurs via the α -hydroxybenzyl ($\bullet\text{CH}(\text{OH})\text{Ph}$) free radical mechanism. Density functional theory (DFT) calculations manifest that the moderate adsorption of $\bullet\text{CH}(\text{OH})\text{Ph}$ radical on the CdS/TNS interface could lead to the high selectivity of C-C coupled products. This work would be anticipated to inspire new insights to design rational cooperative photoredox systems of coupling selective organic transformations with CO_2 valorization by means of synergistic utilization of photoexcited electrons and holes.

2. Experimental section

2.1. Materials

Tetrabutyl titanate ($\text{Ti}(\text{OBu})_4$, 98%), hydrofluoric acid (HF, 47%), sulphur, N, N-dimethylformamide ($\text{C}_3\text{H}_7\text{NO}$), acetone, methanol and ethanol ($\text{C}_2\text{H}_6\text{O}$) were obtained from Sinopharm Chemical Reagent Co., Ltd. (Shanghai, China). Branched polyethylenimine ($M_w \sim 25000$, BPEI), 1-octadecene and oleic acid were obtained from Sigma-Aldrich. 3-mercaptopropionic acid (MPA), tetramethylammonium hydroxide, cadmium oxide (CdO), benzyl alcohol, benzaldehyde, hydrobenzoin, 5, 5-dimethyl-1-pyrroline N-oxide and benzoin were supplied by Aladdin Biochemical Technology Co. Ltd. (Shanghai, China).

2.2. Synthesis

2.2.1. Synthesis of TiO_2 Nanosheets (TNS)

Anatase TiO_2 TNS were prepared by a facile solvothermal method [28]. Detailed preparation procedures can be found in the supporting information (SI).

2.2.2. Synthesis of CdS quantum dots (QDs)

CdS QDs were prepared by a hot-injection method [29,30]. Typically, a mixture of 1-octadecene (36 mL), oleic acid (5 mL), and CdO (3 mmol) was heated to 280 °C. A solution of sulphur (1.5 mmol) was swiftly injected into above solution. Then, the mixture was cooled down to 220 °C and maintained for 1 h. After being cooled down, the product was purified with acetone, and then re-dispersed in chloroform. Ligand exchange with MPA was performed in the light of a previous report [31]. 1 mL of MPA was dispersed in 20 mL of chloroform/methanol and the pH value was adjusted to about 11 with tetramethylammonium hydroxide. The obtained CdS QDs (30 mg) were added into the above mixture and stirred in the dark overnight. Subsequently, the CdS QDs were aggregated and washed with acetone, and finally re-dispersed in

water.

2.2.3. Synthesis of CdS/TNS composites

To functionalize the obtained TNS with positive charge, 0.4 g of TNS was dispersed in 200 mL of ethanol, followed by adding 350 mg of BPEI, which were heated at 60 °C for 4 h. The BPEI-TNS was isolated by centrifugation, washed with deionized water repeatedly, and finally dried in air. 0.1 g of BPEI-TNS was dispersed in 100 mL of deionized water. Then, a certain amount of CdS -MPA was added dropwise to this dispersion and stirred for 1 h. Subsequently, this mixture was transferred into a Teflon autoclave and then kept at 180 °C for 4 h. The acquired sediment was separated by filtration and dried in an oven at 60 °C. The CdS/TNS composites with different CdS weight loading (10, 20 and 30 wt%) were obtained.

2.3. Photoactivity testing

In a typical process, 5 mg as-synthesized sample was added into 5 mL CH_3CN containing 0.1 mmol BA. Subsequently, the reaction solution was sonicated for 5 min, and then purged with CO_2 for 20 min to ensure the full dissolution of CO_2 . Finally, a 300 W Xe lamp (PLS-SXE 300D, Beijing Perfectlight Co., Ltd) with a light power density of 0.8 W cm^{-2} was used as the irradiation source. The evolved H_2/CO was analysed using a gas chromatograph (Shimadzu GC-2014 C). The liquid products were analysed by the high performance liquid chromatography (Shimadzu HPLC-LC20AT). In the isotope-labeling experiment, $^{12}\text{CO}_2$ was replaced by $^{13}\text{CO}_2$. The formation of ^{13}CO was analyzed by a gas chromatograph-mass spectra (Shimadzu GC-MS QP 2020). The gas products were measured by the production rate of the product within a certain time period under visible light irradiation by per gram of catalyst (Eq. 1).

$$R(\text{CO, H}_2) = \frac{n(\text{CO, H}_2)}{m(\text{catalyst})} \quad (1)$$

The conversion of BA and selectivity of BAD, hydrobenzoin and benzoin were calculated using the following equations:

$$\text{Conversion of BA} = \frac{C_0 - C_{\text{BA}}}{C_0} \times 100\% \quad (2)$$

$$\text{Selectivity of BAD} = \frac{C_{\text{BAD}}}{C_{\text{BAD}} + C_{\text{C-C}}} \times 100\% \quad (3)$$

$$\text{Selectivity of C-C} = \frac{C - C}{C_{\text{BAD}} + C_{\text{C-C}}} \times 100\% \quad (4)$$

where C_0 is the initial concentration of BA; C_{BA} , C_{BAD} , and $C_{\text{C-C}}$ are the concentrations of the residual BA and the products after the reaction, respectively.

3. Results and discussion

3.1. Synthesis and morphology

Fig. 1a displays the synthesis procedure for zero-dimensional CdS QDs-two-dimensional TiO_2 NSs (CdS/TNS). Firstly, the solvothermally synthesized TiO_2 NSs (TNS) are functionalized by branched polyethylenimine (BPEI) to be positively charged (Fig. S1a) [28], while CdS quantum dots (QDs) are inherently negatively charged owing to the presence of 3-mercaptopropionic acid (MPA) after the ligand exchange process (Fig. S1b) [25]. The electrostatic interaction force between TNS-BPEI with the Zeta potential (ξ) of + 30.2 mV and CdS QDs with ξ of - 47.8 mV allows the fabrication of CdS/TNS composites via an electrostatic self-assembly process. Subsequently, the hydrothermal method has been employed to strengthen the interaction between the CdS QDs and TNS.

Transmission electron microscopy (TEM) is utilized to examine the

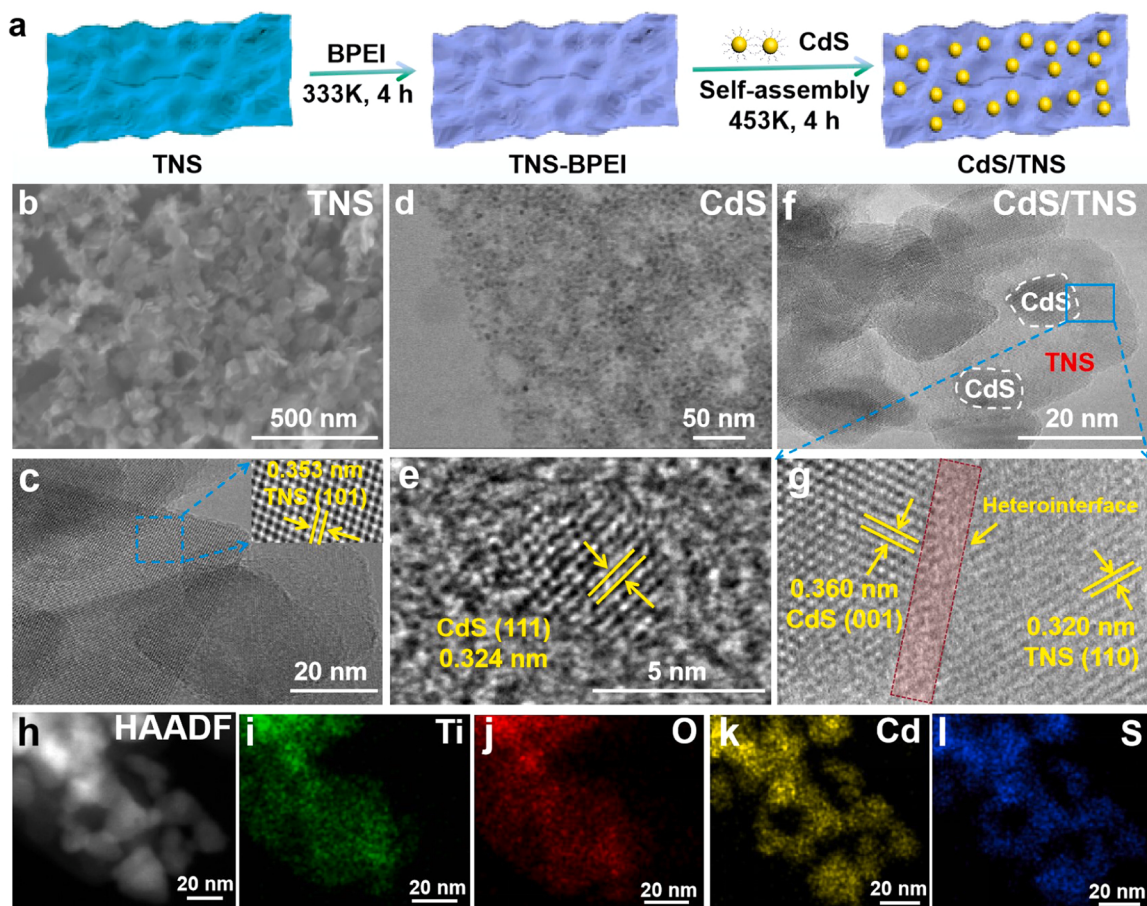


Fig. 1. (a) The flowchart of CdS/TNS composite preparation. (b, c) TEM images for bare TNS; inset of (c) is the HRTEM image of TNS. TEM and HRTEM images for (d, e) CdS QDs and (f, g) CdS/TNS composites. (h-l) element mapping results of CdS/TNS composites.

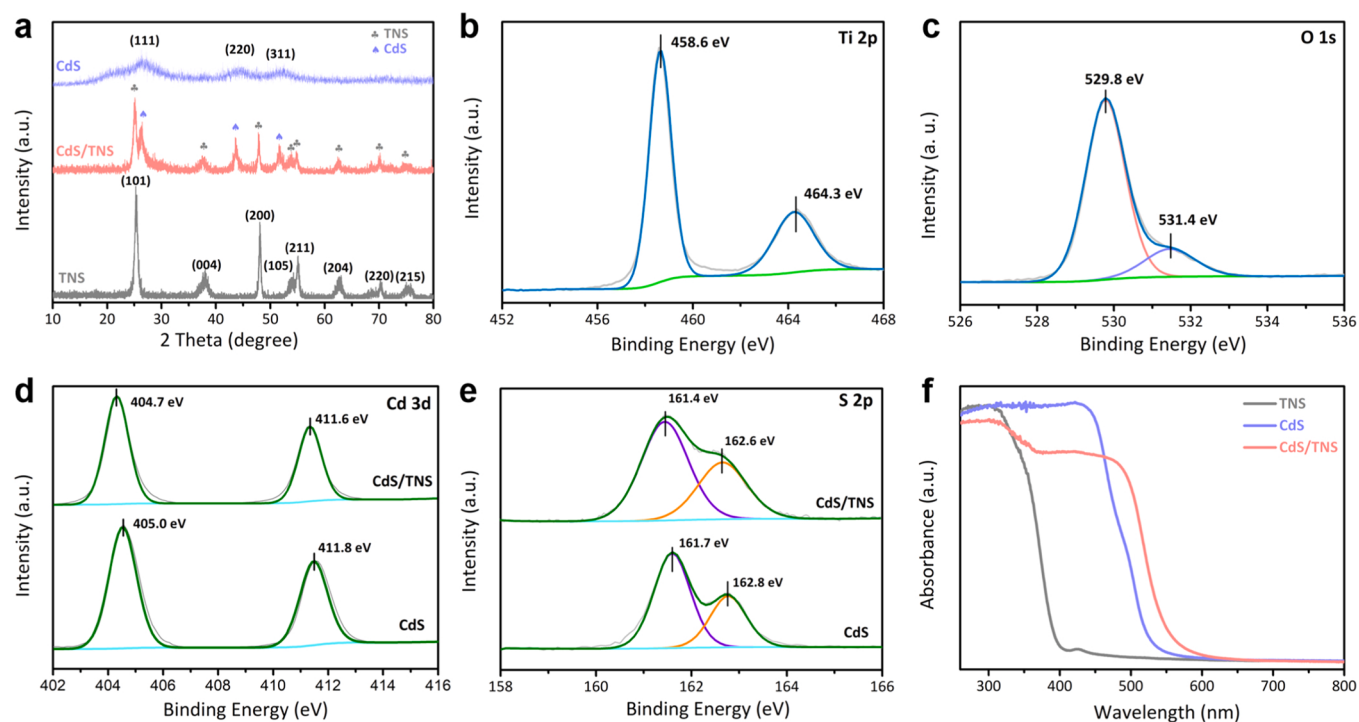


Fig. 2. (a) XRD of TNS, CdS QDs and CdS/TNS composites. High-resolution XPS spectra of (b) Ti 2p and (c) O 1s of CdS/TNS composite. High-resolution XPS spectra of (d) Cd 3d and (e) S 2p of CdS QDs and CdS/TNS composite. (f) DRS of TNS, CdS QDs and CdS/TNS composite.

microscopic structures and morphologies of these samples. The well-defined nanosheet structures of TNS can be observed in Fig. 1b and c, and the lattice fringe of 0.353 nm is indexed to the (101) plane of TNS (inset of Fig. 1c) [2]. The TEM images in Fig. 1d and e demonstrate the nanoparticle structure of CdS and the lattice fringe of 0.324 nm corresponds to the (111) plane of CdS [25]. Fig. 1f displays the TEM image of CdS/TNS composites, implying the intimate interfacial contact between CdS QDs and TNS. From the high-resolution TEM (HRTEM) image in Fig. 1g, both the lattice fringe of 0.360 nm corresponding to the (001) plane of CdS, and that of 0.320 nm corresponding to the (110) plane of TNS are clearly observed. A crystal fusion domain with strong lattice distortions is formed between the phase edge of CdS QDs and TNS, implying the robust interfacial interaction between TNS and CdS QDs (Fig. 1g). These results indicate the successful introduction of CdS QDs onto TNS, and the intimate interfacial interaction formed between themselves. Furthermore, the elemental mapping certifies the elemental distribution of CdS/TNS composites. The elements of Ti, O, Cd and S are uniformly distributed in the CdS/TNS composites (Fig. 1h-l), suggesting that CdS QDs are successfully anchored on TNS.

3.2. Physicochemical properties

X-ray diffraction (XRD) has been carried out to investigate the lattice structure of these samples. As shown in Fig. 2a, the pure TNS shows several diffraction peaks located at 25.3, 37.8, 48.0, 53.9, 55.1, 62.7, 70.3 and 75.0°, which are assigned to the (101), (004), (200), (105), (211), (204), (220) and (215) facets of the anatase phase of TiO_2 (JCPDS No. 21-1272), respectively [2]. The bare CdS QDs show that the characteristic peaks at 26.5, 44.0 and 52.1° are assigned to the (111), (220) and (311) lattice planes of cubic CdS (JCPDS No. 75-0581), respectively [25]. As for CdS/TNS composites, the characteristic diffraction peaks of CdS and TNS are clearly distinguished in the composites.

The elemental compositions and valence states of CdS/TNS composites are analyzed by X-ray photoelectron spectroscopy (XPS, Fig. S3). In Fig. 2b, two peaks located at 458.6 and 464.3 eV in the Ti 2p spectrum are attributed to Ti 2p_{3/2} and Ti 2p_{1/2}, respectively [2]. The peak appearing at 529.8 eV in the O 1s spectrum (Fig. 2c) is assigned to Ti–O bond in TiO_2 [32], and surface hydroxyl group contributes to the peak at 531.4 eV [28]. In Fig. 2d, the binding energies of Cd 3d_{5/2} at 405.2 eV and Cd 3d_{3/2} at 411.9 eV are attributed to Cd²⁺ [33–35]. The peaks at 161.6 and 162.8 eV in Fig. 2e are characteristic of the S²⁻ [34,36]. Significantly, the binding energies of Cd 3d and S 2p characteristic peaks in CdS/TNS composite slightly move to lower values compared with bare CdS, revealing the strong electronic interaction between CdS and TNS [37,38]. Moreover, the optical absorption capacities of various samples have been analyzed by UV-vis diffuse reflectance spectra (DRS). As sketched in Fig. 2f, TNS shows a characteristic absorption edge at wavelength of 400 nm, correlating with the intrinsic band gap of TiO_2 [33], while CdS shows a remarkable absorption edge at wavelength of 500 nm [39]. For CdS/TNS composite, addition of CdS results in a strong and broad absorption in the visible light region.

3.3. Photoredox reaction and mechanism of CO_2 reduction with oxidation of benzyl alcohol

Subsequently, these samples are utilized for a cooperative catalytic system toward carbon dioxide (CO_2) photoreduction integrated with selective oxidation of benzyl alcohol (BA) under the irradiation of visible light ($\lambda > 420$ nm). The activity comparison of as-prepared samples under different conditions is shown in Table 1. As disclosed in entry 1, owing to the fact that TNS cannot be band-gap excited by visible light, no gas-phase and liquid-phase products are detected over bare TNS. A low photoactivity for the conversion of BA to benzaldehyde (BAD) appears on bare CdS QDs (entry 2). Notably, the introduction of CdS QDs onto TNS not only triggers the photoreduction of CO_2 into carbon monoxide (CO), but also tunes the selectivity for the oxidation of BA.

Table 1

Photocatalytic BA oxidation integrated with CO_2 reduction under different conditions^a.

Entry	catalyst	CO yield ($\mu\text{mol g}^{-1}$)	H_2 yield ($\mu\text{mol g}^{-1}$)	BA conversion (%)	BAD selectivity (%)	C–C products selectivity (%)
1	TNS	n.d.	n.d.	n.d.	n.d.	n.d.
2	CdS	n.d.	n.d.	10.6	99.9	n.d.
3	CdS/ TNS	18.6	51.6	27.9	5.1	94.9
4	None	n.d.	n.d.	n.d.	n.d.	n.d.
5 ^b	CdS/ TNS	n.d.	n.d.	0.5	99.9	n.d.
6 ^c	CdS/ TNS	1.6	69.5	16.2	10.9	89.7
7 ^d	CdS/ TNS	7.2	8.2	30.1	36.4	64.6
8 ^e	CdS/ TNS	17.9	n.d.	6.1	99.9	n.d.

n.d. means not detected.

^a Reaction conditions: 5 mg catalyst, 5 mL CH_3CN , 0.1 mmol BA, 1 atm CO_2 , room temperature, visible light ($\lambda > 420$ nm), 2 h.

^b without light irradiation,

^c Ar instead of CO_2 ,

^d CCl_4 as electron scavenger was added,

^e TEOA as hole scavenger was added. C–C products include benzoin and hydrobenzoin.

The yields of CO and hydrogen (H_2) over CdS/TNS composite with optimal CdS loading value of 20 wt% are $18.6 \mu\text{mol g}^{-1}$ and $51.6 \mu\text{mol g}^{-1}$, respectively (entry 3 in Table 1 and Table S1). Moreover, the rate of α -H abstraction at the interface between CdS and TNS is significantly affected by introducing TNS as the support [40], thereby adjusting the selectivity of BA oxidation from BAD (99.9%) to the C–C coupled products (94.9%), among which 94.5% is hydrobenzoin, 0.4% is benzoin. Significantly, the changing trend of apparent quantum yields (AQYs) for CO and H_2 over wavelength (Fig. S4) is well consistent with the DRS spectrum of the CdS/TNS composites, suggesting that the photoreduction of CO_2 is initiated by light excitation of CdS/TNS composites. Furthermore, we have chosen aromatic alcohols with different substituent groups on aryl ring or α -carbon to further evaluate the generality of the dehydrogenative coupling of aromatic alcohols into C–C coupled products integrated with CO_2 reduction. As shown in Table S2, the present system is highly selective (> 91.4%) for the C–C coupled products with different substrate groups. By the removal of light irradiation or photocatalyst, no activity toward CO/ H_2 production is observed, and only a few amount of BAD is generated (entry 4 and 5), manifesting that the dual-functional reaction is a photo-driven process [41]. Upon CO_2 is replaced with argon (Ar), a little CO is detected, indicating that the obtained CO from decomposition of carbon residues is negligible (entry 6) [13]. To further track the carbon source of obtained CO, the isotope experiment is investigated using $^{13}\text{CO}_2$ as the gas feedstock. As shown in Fig. S5, the main signal at $m/z = 29$ in the gas chromatography-mass spectrometry is assigned to ^{13}CO , suggesting that the obtained CO is originated from the photoreduction of CO_2 . The addition of CCl_4 as electron scavenger [42] to the reaction system obviously decreases the yield of CO and H_2 , implying that the photo-generated electrons are the main reductive species for the CO_2 reduction and H_2 evolution. Simultaneously, the trapping of photogenerated electrons with CCl_4 benefits the efficiency of photogenerated holes for oxidation of BA, thereby increasing the BA conversion (entry 7). When triethanolamine (TEOA) as holes sacrificial reagents is added into the reaction [4], the conversion of BA is significantly decreased (entry 8), confirming that the photoexcited holes play a key role for the conversion of BA into C–C coupled products.

To gain more hints on the photocatalytic process of this cooperative reaction system, the electron paramagnetic resonance (EPR) technique

is utilized to detect the active intermediate over the bare CdS QDs and CdS/TNS composite with 5, 5-dimethyl-1-pyrroline-N-oxide (DMPO) as the radical scavenger. As disclosed in Fig. 3a, the typical EPR spectra of the bare CdS QDs and CdS/TNS composite display six characteristic signal peaks with alike intensity under visible light, which belong to the carbon-centered radical intermediate [20]. In addition, the hydrogen and nitrogen hyperfine splittings for the nitroxide nitrogen were measured to be 22.0 and 15.8, respectively, which are in agreement with the previous researches [25,26]. The molecular weight equaled to the adduct of DMPO and $\bullet\text{CH(OH)Ph}$ was also detected in the liquid chromatography-mass (LC-MS) chromatogram (Fig. S6). Furthermore, the signal intensities of DMPO-CH(OH)Ph adduct over CdS/TNS composite are stronger than those for CdS QDs, reflecting that more $\bullet\text{CH(OH)Ph}$ is photogenerated in the CdS/TNS-catalyzed system [18,25]. Therefore, the CdS/TNS composites are obviously conducive to the homocoupling of $\bullet\text{CH(OH)Ph}$ radical.

To further investigate the high selectivity of C–C coupled products at the CdS/TNS interface, density functional theory (DFT) calculations are carried out. The CdS (111) surface model containing 27 Cd and 27 S atoms is used to model the bare CdS QDs, while the Cd₇S₇ cluster resided on the surface of TiO₂ (101) is used to simulate the CdS/TNS composite (Fig. S7a and b). The bond cleavage process of C_α-H over bare CdS and CdS/TNS composites is shown in Fig. 3b and c. Initially, the adsorption energies of BA on CdS/TNS and CdS are -0.70 and -0.44 eV (Fig. 3b and c, Table S3). Then, the molecular hydrogen undergoes dissociative adsorption to form the key intermediate of $\bullet\text{CH(OH)Ph}$ radical. The energy barrier of C_α-H cleavage over the interface of CdS/TNS is 1.46 eV, which is the rate determining step for BA oxidation. In contrast, the energy barrier of C_α-H cleavage over bare CdS QDs is 1.75 eV, implying that the CdS QDs is less active than the CdS/TNS composite. This lower energy barrier indicates the more feasibility of forming $\bullet\text{CH(OH)Ph}$ radicals, and thus contributes to the significantly enhanced

selectivity of C–C coupled products over CdS/TNS. Furthermore, it is noted that the formed $\bullet\text{CH(OH)Ph}$ intermediate has a lower adsorption energy of -1.26 eV on CdS/TNS than that over CdS QDs, and thus can readily desorb from the CdS/TNS surface for producing C–C coupled products (Table S3). However, a strong adsorption of $\bullet\text{CH(OH)Ph}$ is occurred on the bare CdS (-1.77 eV) surface, thereby being beneficial for undergoing consecutive oxidation to form BAD. Hence, the weak adsorption of $\bullet\text{CH(OH)Ph}$ on CdS/TNS should play a key role in the formation of C–C coupled products.

To investigate the stability of CdS/TNS composite, long-time experiments have been conducted. The results of long-term photoactivity test over CdS/TNS composite show that the yields of H₂ and CO increase along with the reaction time (Fig. 3d). After 8 h of visible light irradiation, the conversion of BA is approximately 71% and the selectivity for C–C coupled products reaches 96.8% (95.9% of hydrobenzoin and 0.9% of benzoin). CO and H₂ production yields reach at 60.7 and $128.1 \mu\text{mol g}^{-1}$, while no gas-phase products (CO and H₂) are detected over bare CdS QDs, and the conversion of BA is relatively low (Fig. S8). Fig. S9a illustrates the light-capturing property maintenance in the CdS/TNS composite, reflecting its enhanced anti-photocorrosion ability. Furthermore, XRD profiles and HRTEM images (Fig. S9-11) of CdS/TNS composite before and after long-time experiments certify that the crystalline phase and morphology are well maintained. As presented in Table S4, there is detectable Cd²⁺ leaching in the reaction solution (1.4×10^{-4} mg) after continuous light irradiation of CdS/TNS composite aqueous dispersion for 8 h, which is lower than that of bare CdS QDs (4.9×10^{-4} mg). Therefore, the CdS/TNS composite features enhanced anti-photocorrosion ability and improved durability during photocatalytic process.

Notably, the CO₂ adsorption/desorption performance over the photocatalyst greatly affect the activity of CO₂ photoreduction. The CO₂-temperature-programmed-desorption (TPD) measurements have been

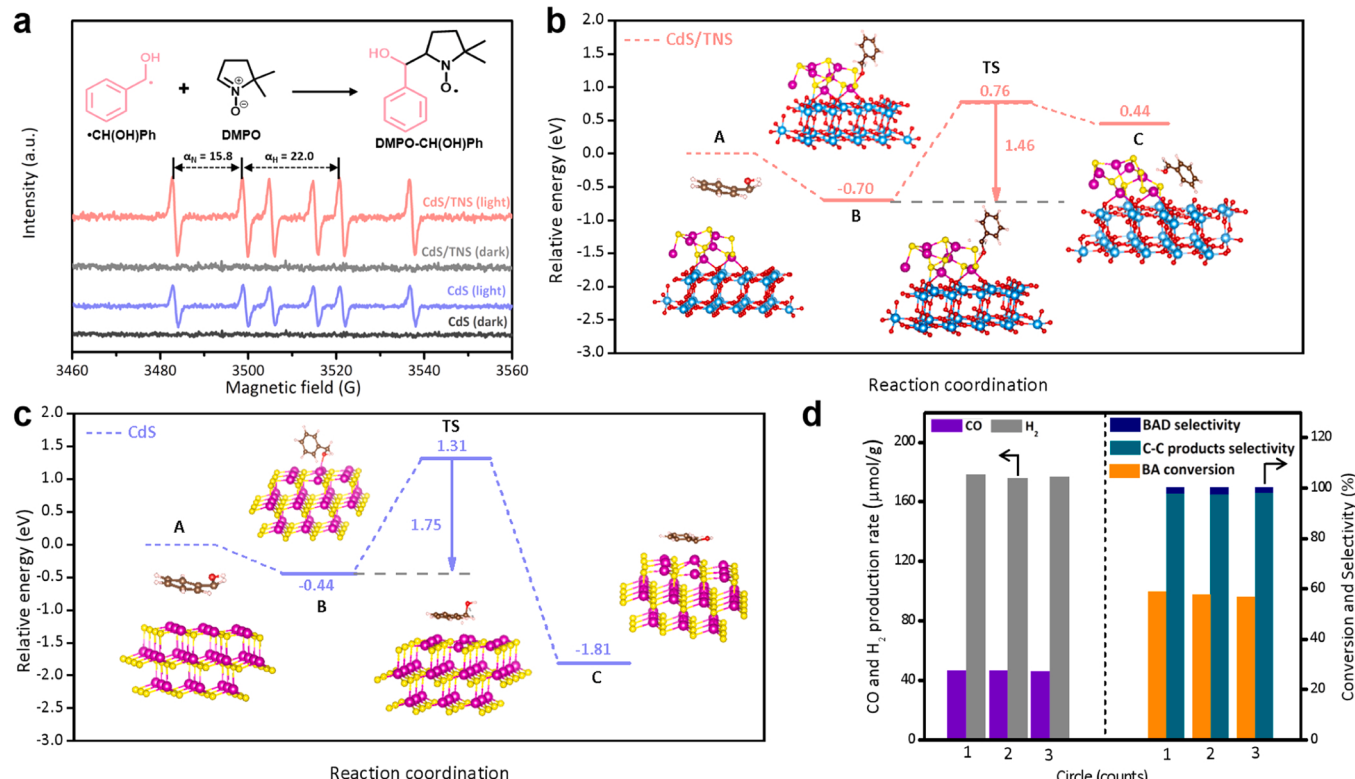


Fig. 3. (a) EPR spectra of bare CdS and CdS/TNS composite in CH₃CN solution with the addition of DMPO. (b) Full potential energy for BA deprotonation on CdS/TNS composite by DFT calculations. Atoms in pink, yellow, blue, red, brown and white represent Cd, S, Ti, O, C and H respectively. (c) Full potential energy for BA deprotonation on CdS QDs by DFT calculations. Atoms in pink, yellow, brown, red and white represent Cd, S, C, O and H respectively. (d) Long-term photoactivity of the dual-functional reaction over CdS/TNS composite.

performed to investigate the CO_2 adsorption capacity of TNS, CdS and CdS/TNS composites (Fig. 4a). There is a strong CO_2 desorption peak with maximum at 350°C in the CO_2 -TPD profile of TNS, suggesting that the surface of TNS could induce a certain extent of the CO_2 adsorption [43]. Compared to TNS, the CO_2 desorption peak of CdS QDs is in higher temperature region ($350\text{--}450^\circ\text{C}$), suggesting that CdS QDs possess more superior CO_2 adsorption capacity than TNS. When introducing CdS QDs onto the surface of TNS, the CO_2 desorption peaks located at $350\text{--}450^\circ\text{C}$ produce considerably strong CO_2 adsorption sites at the interface of CdS/TNS composite [44], whose intensity is higher than that of bare CdS QDs. When the adsorption is enhanced, CO_2 molecules are easily fixed on the surface of catalyst for ensuing CO_2 photoreduction [13]. Moreover, the efficiency of charge carriers separation has been proved by the photoelectrochemical measurements. As shown in Fig. 4b, the CdS/TNS composites exhibit a smallest depressed semicircle at high frequency among three samples, suggesting the more efficient interfacial charge mobility in the CdS/TNS heterostructure [29]. As displayed in Fig. 4c, significantly enhanced photocurrent densities can be achieved over CdS/TNS composite as compared to TNS and CdS, suggesting that the synergy between CdS and TNS effectively promotes the charge transfer within the binary CdS/TNS composite. Additionally, the open-circuit photovoltage and corresponding decay (Fig. S12) analysis show that

CdS/TNS composite discloses a longer electron lifetime than bare TNS and CdS, which is in accordance with the trend of photocurrent response [32,33]. The photoluminescence (PL) spectra have been carried out to probe charge recombination using an excitation wavelength of 405 nm. As shown in Fig. 4d, the PL intensity of CdS/TNS is significantly lower than that of bare CdS QDs, suggesting that the compositing heterointerface between CdS QDs and TNS can effectively weaken the recombination of photoexcited charge carriers [45]. Furthermore, time-resolved PL decay spectra are performed to study the photo-generated charge carrier dynamics (Fig. 4e and Table S5). The decay kinetics of CdS/TNS shows a shorter average emission lifetime (2.9512 ns) than that of CdS (3.9679 ns), implying the faster interface charges transfer in the CdS/TNS composite [46]. These results consolidate that the effective transfer and accumulation of multiple electrons in CdS/TNS composite promote the activity of photoredox-catalyzed BA oxidation coupled with CO_2 reduction.

To probe the catalytic mechanism for photoredox activity over CdS/TNS composite, the band positions of TNS and CdS are identified by the combination of DRS spectra, Mott–Schottky plots, and valence-band XPS spectra [47–49]. Based on the Kubelka–Munk function plots (Fig. 4f), the band-gap energies (E_g) of TNS and CdS are calculated to be 3.24 and 2.51 eV, respectively [25]. According to the valence-band XPS

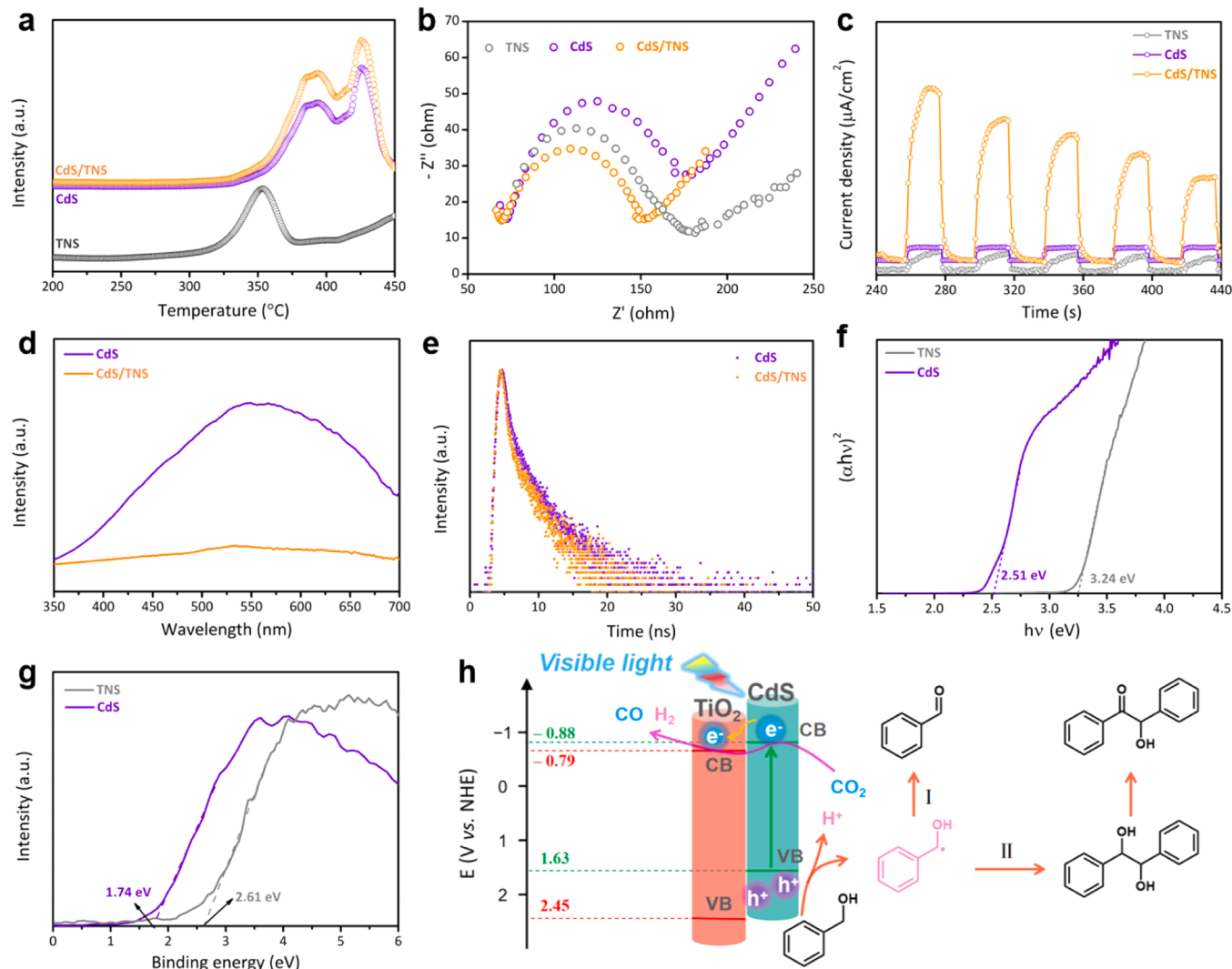


Fig. 4. (a) CO_2 -TPD analysis, (b) Electrochemical impedance spectroscopy (EIS) and (c) Transient photocurrent spectra of TNS, CdS and CdS/TNS composite. (d) Photoluminescence (PL) emission spectra and (e) Time-resolved PL spectra of CdS and CdS/TNS composite. (f) The estimated energy band-gap energies for TNS and CdS obtained by the Kubelka–Munk function plots converted from the DRS spectra. (g) Valence-band XPS spectra of TNS and CdS. (h) Schematic diagram of photocatalytic CO_2 reduction integrated with C–C coupling synthesis.

spectra (Fig. 4g), the energy differences between the valence band maximum and the Fermi level are calculated to be about 2.61 and 1.74 eV for TNS and CdS, respectively [49]. As displayed in Fig. S13, the Mott-Schottky plots indicate the n-type characteristics of TNS and CdS owing to the curves with positive slopes, and their flat band potentials are determined to be -0.357 and -0.307 V vs. Ag/AgCl, respectively. Therefore, the Fermi levels of TNS and CdS are -0.16 and -0.11 V vs. the normal hydrogen electrode (NHE) according to the equation of $E_{\text{NHE}} = E_{\text{Ag/AgCl}} + 0.197$ V [47]. Therefore, the valence band maximum for TNS and CdS are calculated to be 2.45 and 1.63 V vs. NHE, and the conduction band minimum values are calculated to be -0.79 and -0.88 V vs. NHE, respectively (Fig. 4h).

On the basis of the above analyses and results, the photocatalytic mechanism for CO_2 reaction coupling with C–C bond synthesis of CdS/TNS composite is proposed in Fig. 4h. Under visible light illumination, TiO_2 cannot be band-gap excited [50], whereas CdS component in CdS/TNS composite is photoexcited to generate the energetic electrons and holes. The electrons localized from the conduction band of CdS transfer to the conduction band of TNS following the type-II band alignment to drive the dual-function photocatalytic redox processes [33]. Consequently, the charge carriers recombination is effectively decreased, leading to an enhanced photoactivity. The photogenerated holes in the valence band of CdS first oxidize the C–H bond of BA, affording $\bullet\text{CH}(\text{OH})\text{Ph}$ and protons. Then, the $\bullet\text{CH}(\text{OH})\text{Ph}$ radicals can either be further oxidized by holes to produce BAD or couple to form hydrobenzoin, and a small portion of hydrobenzoin is subsequently oxidized to benzoin. Meanwhile, the protons abstracted from BA and CO_2 molecules react with the photoexcited electrons to form H_2 and CO , respectively.

4. Conclusion

In summary, we have reported a cooperative reaction system for CO_2 photoreduction to CO paired with selective BA oxidation in one photocatalytic redox cycle with tunable selectivity under visible light irradiation. The compositing heterointerface between 0D CdS quantum dots and 2D TiO_2 nanosheets not only offers a suitable surface for CO_2 adsorption and activation, but also enables the facile desorption of $\bullet\text{CH}(\text{OH})\text{Ph}$ from the interface of CdS/TNS composites for subsequent C–C coupling, thereby facilitating the formation of CO and significantly improving the selectivity of C–C coupled products. This work is expected to provide a feasible protocol for the rational design of heterostructure composites toward cooperative visible light-driven solar fuel production by CO_2 valorization and organic transformations of fine chemicals.

CRediT authorship contribution statement

Ming-Yu Qi: Investigation, Validation, Writing – review & editing, Formal analysis. **Qiong Lin:** Investigation, Validation, Formal analysis, Writing – review & editing. **Zi-Rong Tang:** Funding acquisition, Formal analysis, Supervision, Writing – review & editing, Resources. **Yi-Jun Xu:** Funding acquisition, Conceptualization, Resources, Project administration, Writing – review & editing, Supervision.

Declaration of Competing Interest

The authors declare that they have no known competing financial interests or personal relationships that could have appeared to influence the work reported in this paper.

Acknowledgements

The support from the National Natural Science Foundation of China (22172030, 22072023, 21872029, and U1463204), the Program for National Science and Technology Innovation Leading Talents

(00387072), the Program for Leading Talents of Fujian Universities, and the 1st Program of Fujian Province for Top Creative Young Talents, and the Natural Science Foundation (2019J0106 and 2017J07002) of Fujian Province is gratefully acknowledged.

Appendix A. Supporting information

Supplementary data associated with this article can be found in the online version at doi:10.1016/j.apcatb.2022.121158.

References

- [1] A. Meng, B. Cheng, H. Tan, J. Fan, C. Su, J. Yu, TiO_2 /polydopamine S-scheme heterojunction photocatalyst with enhanced CO_2 -reduction selectivity, *Appl. Catal. B* 289 (2021), 120039.
- [2] L. Yuan, K.-Q. Lu, F. Zhang, X. Fu, Y.-J. Xu, Unveiling the interplay between light-driven CO_2 photocatalytic reduction and carbonaceous residues decomposition: a case study of Bi_2WO_6 – TiO_2 bimanoths, *Appl. Catal. B* 237 (2018) 424–431.
- [3] X. Hu, Z. Xie, Q. Tang, H. Wang, L. Zhang, J. Wang, Enhanced CH_4 yields by interfacial heating-induced hot water steam during photocatalytic CO_2 reduction, *Appl. Catal. B* 298 (2021), 120635.
- [4] K.-Q. Lu, Y.-H. Li, F. Zhang, M.-Y. Qi, X. Chen, Z.-R. Tang, Y.M.A. Yamada, M. Anpo, M. Conte, Y.-J. Xu, Rationally designed transition metal hydroxide nanosheet arrays on graphene for artificial CO_2 reduction, *Nat. Commun.* 11 (2020) 5181.
- [5] S.N. Habersreuter, L. Schmidt-Mende, J.K. Stolarczyk, Photocatalytic reduction of CO_2 on TiO_2 and other semiconductors, *Angew. Chem. Int. Ed.* 52 (2013) 7372–7408.
- [6] S. Wu, J. Wang, Q. Li, Z. Huang, Z. Rao, Y. Zhou, Bi/BiOCl nanosheets enriched with oxygen vacancies to enhance photocatalytic CO_2 reduction, *Trans. Tianjin Univ.* 27 (2021) 155–164.
- [7] J. Song, Y. Lu, Y. Lin, Q. Liu, X. Wang, W. Su, A direct Z-scheme alpha- Fe_2O_3 / LaTiO_2 visible-light photocatalyst for enhanced CO_2 reduction activity, *Appl. Catal. B* 292 (2021), 120185.
- [8] H.-K. Wu, Y.-H. Li, M.-Y. Qi, Q. Lin, Y.-J. Xu, Enhanced photocatalytic CO_2 reduction with suppressing H_2 evolution via Pt cocatalyst and surface SiO_2 coating, *Appl. Catal. B* 278 (2020).
- [9] K. Li, B. Peng, T. Y, Recent ADVances in Heterogeneous Photocatalytic CO_2 conversion to solar fuels, *ACS Catal.* 6 (2016) 7485–7527.
- [10] J.L. White, M.F. Baruch, J.E. Pander III, Y. Hu, I.C. Fortmeyer, J.E. Park, T. Zhang, K. Liao, J. Gu, Y. Yan, T.W. Shaw, E. Abelev, A.B. Bocarsly, Light-driven heterogeneous reduction of carbon dioxide: photocatalysts and photoelectrodes, in: *Chem. Rev.* 115, 2015, pp. 12888–12935.
- [11] S. Wang, X. Han, Y. Zhang, N. Tian, T. Ma, H. Huang, Inside-and-out semiconductor engineering for CO_2 photoreduction: from recent advances to new trends, *Small Struct.* 2 (2021), 2000061.
- [12] Xiao Liu, Shinji Inagaki, J. Gong, Heterogeneous molecular systems for photocatalytic CO_2 reduction with water oxidation, *Angew. Chem. Int. Ed.* 55 (2016) 14924–14950.
- [13] C. Han, Y.-H. Li, J.-Y. Li, M.-Y. Qi, Z.-R. Tang, Y.-J. Xu, Cooperative syngas production and C–N bond formation in one photoredox cycle, *Angew. Chem. Int. Ed.* 60 (2021) 7962–7970.
- [14] M.R. Hoffmann, J.A. Moss, M.M. Baum, Artificial photosynthesis: semiconductor photocatalytic fixation of CO_2 to afford higher organic compounds, *Dalton Trans.* 40 (2011) 5151–5158.
- [15] L. Yuan, M.-Y. Qi, Z.-R. Tang, Y.-J. Xu, Coupling strategy for CO_2 valorization integrated with organic synthesis by heterogeneous photocatalysis, *Angew. Chem. Int. Ed.* 60 (2021) 21150–21172.
- [16] Y. Ide, R. Ogino, M. Sadakane, T. Sano, Effects of Au loading and CO_2 addition on photocatalytic selective phenol oxidation over TiO_2 -supported Au nanoparticles, *ChemCatChem* 5 (2013) 766–773.
- [17] M.-Y. Qi, M. Conte, M. Anpo, Z.-R. Tang, Y.-J. Xu, Cooperative coupling of oxidative organic synthesis and hydrogen production over semiconductor-based photocatalysts, *Chem. Rev.* 121 (2021) 13051–13085.
- [18] Q. Lin, Y.-H. Li, M.-Y. Qi, J.-Y. Li, Z.-R. Tang, M. Anpo, Y.M.A. Yamada, Y.-J. Xu, Photoredox dual reaction for selective alcohol oxidation and hydrogen evolution over nickel surface-modified ZnIn_2S_4 , *Appl. Catal. B* 271 (2020), 118946.
- [19] C. Han, Z.-R. Tang, J. Liu, S. Jin, Y.-J. Xu, Efficient photoredox conversion of alcohol to aldehyde and H_2 by heterointerface engineering of bimetal–semiconductor hybrids, *Chem. Sci.* 10 (2019) 3514–3522.
- [20] D. Jiang, X. Chen, Z. Zhang, L. Zhang, Y. Wang, Z. Sun, R.M. Irfan, P. Du, Highly efficient simultaneous hydrogen evolution and benzaldehyde production using cadmium sulfide nanorods decorated with small cobalt nanoparticles under visible light, *J. Catal.* 357 (2018) 147–153.
- [21] Z. Chai, T.-T. Zeng, Q. Li, L.-Q. Lu, W.-J. Xiao, D. Xu, Efficient visible light-driven splitting of alcohols into hydrogen and corresponding carbonyl compounds over a Ni-modified CdS photocatalyst, *J. Am. Chem. Soc.* 138 (2016) 10128–10131.
- [22] J.-Y. Li, X. Xin, Y.-H. Li, F. Zhang, M. Anpo, Y.-J. Xu, Visible light-induced conversion of biomass-derived chemicals integrated with hydrogen evolution over 2D Ni_2P –graphene– TiO_2 , *Res. Chem. Intermed.* 45 (2019) 5935–5946.

- [23] Kevin P. McClelland, E.A. Weiss, Selective photocatalytic oxidation of benzyl alcohol to benzaldehyde or C–C coupled products by visible-light-absorbing quantum dots, *ACS Appl. Energy Mater.* 2 (2018) 92–96.
- [24] N. Luo, T. Hou, S. Liu, B. Zeng, J. Lu, J. Zhang, H. Li, F. Wang, Photocatalytic coproduction of deoxybenzoin and H₂ through tandem redox reactions, *ACS Catal.* 10 (2019) 762–769.
- [25] M.-Y. Qi, Y.-H. Li, M. Anpo, Z.-R. Tang, Y.-J. Xu, Efficient photoredox-mediated C–C coupling organic synthesis and hydrogen production over engineered semiconductor quantum dots, *ACS Catal.* 10 (2020) 14327–14335.
- [26] Q. Guo, F. Liang, X.-B. Li, Y.-J. Gao, M.-Y. Huang, Y. Wang, S.-G. Xia, X.-Y. Gao, Q.-C. Gan, Z.-S. Lin, C.-H. Tung, L.-Z. Wu, Efficient and selective CO₂ reduction integrated with organic synthesis by solar energy, *Chem* 5 (2019) 2605–2616.
- [27] G. Han, X. Liu, Z. Cao, Y. Sun, Photocatalytic pinacol C–C coupling and jet fuel precursor production on ZnIn₂S₄ nanosheets, *ACS Catal.* 10 (2020) 9346–9355.
- [28] B. Weng, J. Zhang, Z.-F. Shi, Z. Tang, L.-S. Zheng, Y.-J. Xu, Improving the photostability of ultrasmall Au clusters via a combined strategy of surface engineering and interfacial modification, *Langmuir* 35 (2019) 5728–5736.
- [29] X. Wu, S. Xie, C. Liu, C. Zhou, J. Lin, J. Kang, Q. Zhang, Z. Wang, Y. Wang, Ligand-controlled photocatalysis of CdS quantum dots for lignin valorization under visible light, *ACS Catal.* 9 (2019) 8443–8451.
- [30] X. Wu, X. Fan, S. Xie, J. Lin, J. Cheng, Q. Zhang, L. Chen, Y. Wang, Solar energy-driven lignin-first approach to full utilization of lignocellulosic biomass under mild conditions, *Nat. Catal.* 1 (2018) 772–780.
- [31] T. Yao, Q. Zhao, Z. Qiao, F. Peng, H. Wang, H. Yu, C. Chi, J. Yang, Chemical synthesis, structural characterization, optical properties, and photocatalytic activity of ultrathin ZnSe nanorods, *Chemistry* 17 (2011) 8663–8670.
- [32] M.-Y. Qi, Y.-H. Li, F. Zhang, Z.-R. Tang, Y. Xiong, Y.-J. Xu, Switching light for site-directed spatial loading of cocatalysts onto heterojunction photocatalysts with boosted redox catalysis, *ACS Catal.* 10 (2020) 3194–3202.
- [33] Y.-S. Xie, L. Yuan, N. Zhang, Y.-J. Xu, Light-tuned switching of charge transfer channel for simultaneously boosted photoactivity and stability, *Appl. Catal. B* 238 (2018) 19–26.
- [34] J.-Y. Li, Y.-H. Li, F. Zhang, Z.-R. Tang, Y.-J. Xu, Visible-light-driven integrated organic synthesis and hydrogen evolution over 1D/2D CdS-Ti₃C₂T_x MXene composites, *Appl. Catal. B* 269 (2020), 118783.
- [35] J. Low, B. Dai, T. Tong, C. Jiang, J. Yu, In situ irradiated X-Ray photoelectron spectroscopy investigation on a direct Z-scheme TiO₂/CdS composite film photocatalyst, *Adv. Mater.* 31 (2019), 1802981.
- [36] Y.-H. Li, F. Zhang, Y. Chen, J.-Y. Li, Y.-J. Xu, Photoredox-catalyzed biomass intermediate conversion integrated with H₂ production over Ti₃C₂T_x/CdS composites, *Green. Chem.* 22 (2020) 163–169.
- [37] Z. Lian, P. Xu, W. Wang, D. Zhang, S. Xiao, X. Li, G. Li, C₆₀-decorated CdS/TiO₂ mesoporous architectures with enhanced photostability and photocatalytic activity for H₂ evolution, *ACS Appl. Mater. Interfaces* 7 (2015) 4533–4540.
- [38] J. Wang, S. Sun, H. Ding, W. Li, X. Wang, Well-designed CdS/TiO₂/MS-SiO₂ Z-scheme photocatalyst for combating poison with poison, *Ind. Eng. Chem. Res.* 59 (2020) 7659–7669.
- [39] Y.-H. Li, M.-Y. Qi, J.-Y. Li, Z.-R. Tang, Y.-J. Xu, Noble metal free CdS@CuS-Ni_xP hybrid with modulated charge transfer for enhanced photocatalytic performance, *Appl. Catal. B* 257 (2019).
- [40] C.R. Ho, V. Defalque, S. Zheng, A.T. Bell, Propanol amination over supported nickel catalysts: reaction mechanism and role of the support, *ACS Catal.* 9 (2019) 2931–2939.
- [41] N. Luo, M. Wang, H. Li, J. Zhang, T. Hou, H. Chen, X. Zhang, J. Lu, F. Wang, Visible-light-driven self-hydrogen transfer hydrogenolysis of lignin models and extracts into phenolic products, *ACS Catal.* 7 (2017) 4571–4580.
- [42] S. Meng, X. Ning, S. Chang, X. Fu, X. Ye, S. Chen, Simultaneous dehydrogenation and hydrogenolysis of aromatic alcohols in one reaction system via visible-light-driven heterogeneous photocatalysis, *J. Catal.* 357 (2018) 247–256.
- [43] J. Shan, F. Raziq, M. Humayun, W. Zhou, Y. Qu, G. Wang, Y. Li, Improved charge separation and surface activation via boron-doped layered polyhedron SrTiO₃ for co-catalyst free photocatalytic CO₂ conversion, *Appl. Catal. B* 219 (2017) 10–17.
- [44] L. Lin, K. Wang, K. Yang, X. Chen, X. Fu, W. Dai, The visible-light-assisted thermocatalytic methanation of CO₂ over Ru/TiO₂–N_x, *Appl. Catal. B* 204 (2017) 440–455.
- [45] Y.-H. Chen, M.-Y. Qi, Y.-H. Li, Z.-R. Tang, T. Wang, J. Gong, Y.-J. Xu, Activating two-dimensional Ti₃C₂T_x-MXene with single-atom cobalt for efficient CO₂ photoreduction, *Cell Rep. Phys. Sci.* 2 (2021), 100371.
- [46] K.-Q. Liu, Y.-H. Li, F. Zhang, M.-Y. Qi, X. Chen, Z.-R. Tang, Y.M.A. Yamada, M. Anpo, M. Conte, Y.-J. Xu, Rationally designed transition metal hydroxide nanosheet arrays on graphene for artificial CO₂ reduction, *Nat. Commun.* 11 (2020) 5181.
- [47] Y. Xi, W. Chen, W. Dong, Z. Fan, K. Wang, Y. Shen, G. Tu, S. Zhong, S. Bai, Engineering an interfacial facet of S-scheme heterojunction for improved photocatalytic hydrogen evolution by modulating the internal electric field, *ACS Appl. Mater. Interfaces* 13 (2021) 39491–39500.
- [48] Q. Liu, S. Wang, Q. Ren, T. Li, G. Tu, S. Zhong, Y. Zhao, S. Bai, Stacking design in photocatalysis: synergizing cocatalyst roles and anti-corrosion functions of metallic MoS₂ and graphene for remarkable hydrogen evolution over CdS, *J. Mater. Chem. A* 9 (2021) 1552–1562.
- [49] X. Xue, H. Chen, Y. Xiong, R. Chen, M. Jiang, G. Fu, Z. Xi, X.L. Zhang, J. Ma, W. Fang, Z. Jin, Near-infrared-responsive photo-driven nitrogen fixation enabled by oxygen vacancies and sulfur doping in black TiO₂–S_y nanoplatelets, *ACS Appl. Mater. Interfaces* 13 (2021) 4975–4983.
- [50] J.-Y. Li, Y.-H. Li, M.-Y. Qi, Q. Lin, Z.-R. Tang, Y.-J. Xu, Selective organic transformations over cadmium sulfide-based photocatalysts, *ACS Catal.* 10 (2020) 6262–6280.